applied optics

Axial shift mapping: a self-referencing test for measuring the axial figure of near-cylindrical surfaces

HAYDEN J. WISNIEWSKI,[1] ![ORCID] RALF K. HEILMANN,[2] ![ORCID] MARK L. SCHATTENBURG,[2] ![ORCID] AND BRANDON D. CHALIFOUX[1,*] ![ORCID]

[1] *James C. Wyant College of Optical Sciences, The University of Arizona, 1630 E University Blvd., Tucson, Arizona 85719, USA*
[2] *Kavli Institute for Astrophysics and Space Research, Massachusetts Institute of Technology, 70 Vassar St., Cambridge, Massachusetts 02139, USA*
*bchal@optics.edu

Lateral shearing self-referencing interferometry methods shift the surface under test between measurements to separate its topography from that of the reference surface. However, rigid body errors occur during shifting, creating an ambiguity in the quadratic term of the extracted surfaces. We present axial shift mapping, a lateral shearing self-referencing interferometry method for cylinders, in which the quadratic ambiguity is resolved by measuring the rigid body errors using known artifact mirrors residing in the interferometer's field of view. First, one-dimensional lines of a flat mirror are measured with 2.8 nm RMS difference compared to a three flat test. Then, axial shift mapping is extended to cylindrical surfaces using a computer generated hologram. We find that axial shift mapping results in full surface extraction of cylindrical optics, along the axial direction, with a repeatability of 4.4 nm RMS. We also find that the reference surface extracted through axial shift mapping is within 4.5 nm RMS of the transmitted wavefront error of the computer generated hologram substrate, which was expected to be the largest contribution of reference wavefront error. © 2023 Optica Publishing Group

https://doi.org/10.1364/AO.504270

1. INTRODUCTION

Fizeau interferometry is a foundational method for measuring the surface figure of optical surfaces with high precision. The core principle of Fizeau interferometry is comparing the optical path length difference (OPD) between a wavefront reflected off of a reference surface against a wavefront reflected off of a surface under test (SUT), which are separated by an optical cavity [1] (Fig. 1). Flat and spherical reference surfaces (transmission flats and transmission spheres, respectively) are commonly characterized to $\lambda/20$ peak to valley (PV), which can be assumed as ground truth for most measurements [2]. However, when the desired measurement uncertainty is below this level, other methods must be used to measure the surface. This issue is compounded when measuring surfaces that deviate from a sphere, as null optics are introduced to allow for the measurement. These null optics lie within the cavity, adding errors that increase uncertainty in the OPD, which in turn leads to increased uncertainty in the measurement of the SUT. Self-referencing tests allow the extraction of the true SUT surface figure without direct influence from the uncertainty of the null optics or reference surface. Here we present axial shift mapping (ASM), a self-referencing surface metrology technique aimed at
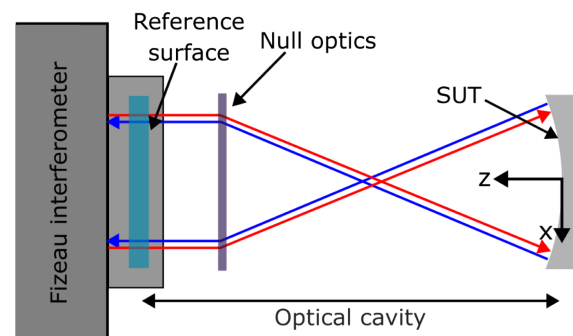

Fig. 1. Fizeau interferometer measuring a curved surface. The null optics, which include the reference surface, create a wavefront intended to match the surface under test (SUT). Any surface deviations will be imprinted on the reflected wavefront through an optical path difference (OPD). This OPD directly relates to extracted surface height.

extracting the axial surface figure of a cylindrical SUT from a set of Fizeau measurements without the effect of the null optics.

Well known self-referencing Fizeau metrology methods, otherwise known as absolute tests or error separation techniques, typically use symmetry to extract information about the SUT

without influence from the reference surface, and vice versa. For example, the three flat test [2] uses a central line of symmetry to extract a single line of information from all three flats. This method can be expanded to a full surface through an n-position test [3], and similar methods exist for spherical surfaces [4].

Lateral shear methods are a self-referencing alternative to the symmetry tests [5–7]. A series of measurements is taken where surfaces are shifted and/or rotated by known amounts. During these shifts, contributions to the interferogram due to the reference surface are static, while contributions due to the SUT will move with the shift. Using this information, the reference surface and the SUT can be extracted from the measurement. This study describes a lateral shear self-referencing method for cylindrical surfaces, with a primary application aimed at expanding reliable metrology methods for X-ray telescope mirrors, which have acylindical profiles. Lateral shear type self-referencing methods have been expanded to cylindrical surfaces in the past [8], but a key challenge with using lateral shear methods for measuring 2D non-flat surfaces, such as X-ray telescope mirrors, is accounting for the quadratic ambiguities [9,10] that arise due to rigid body errors—a challenge that ASM addresses. For cylindrical surfaces, two rigid body error rotations affect the quadratic term along the axial profile, namely, pitch (rotations around x) and roll (rotations around z). Other rigid body error motions do not affect axial figure measurement. Two known artifact mirrors (KAMs) break the quadratic ambiguity by being placed in the field of view of the interferometer to measure both pitch and roll.

X-ray telescope mirrors are off-axis parabaloids and hyperboloids that reflect X-rays at glancing incidence, a rendering of which can be seen in Fig. 2 [11]. Modern segmented X-ray mirrors are typically 100×100 mm with a sagittal curvature range of 130 mm to over 1 m [12]. X-ray telescopes typically have 10 m focal lengths. While X-rays reflect off the mirrors at glancing incidence (i.e., at small angles to the y-axis in Fig. 2), the mirrors are more easily measured near normal incidence (i.e., along the z-axis), making the mirrors nearly cylindrical. Axial figure error [i.e., surface figure error along the optical axis (y) direction of the telescope] degrades imaging performance far more than figure errors along the sagittal direction [13]. The nominal figure is typically dominated by a quadratic figure term that must be tightly controlled for all telescope mirrors to have a common focal length [11]. X-ray telescope optics present particular metrology challenges: they have large sagittal curvature and cannot be bent during operation, in contrast to most X-ray synchroton optics [14,15].

For the next generation of high-resolution X-ray telescopes (Fig. 2) to have sub-arcsecond angular resolution (half-power diameter), they require mirrors with axial figure error around 5 nm RMS. Beyond this, X-ray telescopes and interferometers with micro-arcsecond resolution are being designed [16–18] that would require an axial figure of $\lambda/200$ RMS (at $\lambda = 633$ nm) for the 1.2 keV = (1 nm) X-ray band and $\lambda/1000$ RMS for the 6 keV = (0.2 nm) X-ray band [18]. To achieve this with Fizeau interferometry, it will be necessary to either characterize the null optics to below these levels or implement a self-referencing method that extracts the surface under test (SUT) without influence from the reference surface and null optics.
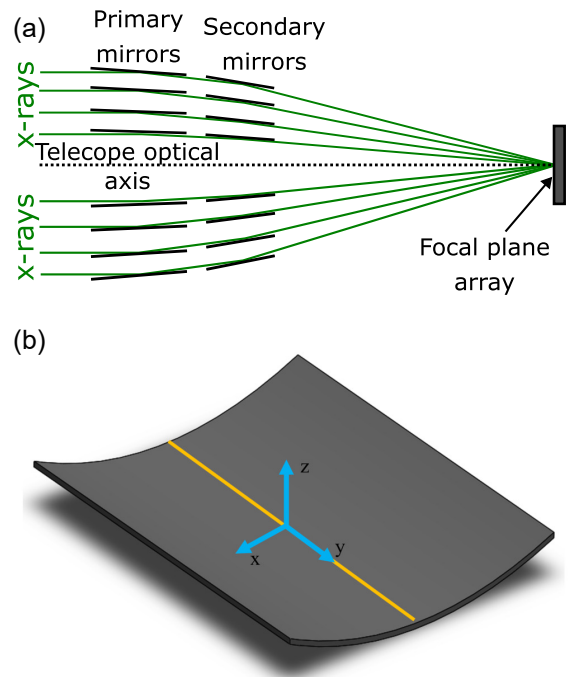

Fig. 2. Axial shift mapping (ASM) may be applied to improve X-ray telescope mirror metrology. (a) Wolter type 1 X-ray telescope. The primary mirror is composed of nested off-axis parabolas, and the secondary mirror is composed of nested off-axis hyperbolas. A ring can be separated into many segments that are then assembled and aligned. (b) Single X-ray telescope mirror segment shown with the mirror coordinate frame used in this paper, in which the y-axis is approximately parallel to the telescope optical axis. The axial profile, traced for one azimuthal position as the orange line along the y direction, is crucial for system performance. The axial profile error, including the quadratic term, must be measured to <5 nm RMS for next generation X-ray telescopes.

One challenge in using Fizeau interferometry for the measurement of near-cylindrical surfaces is generating the test wavefront, which must approximately match the SUT (see Fig. 1). For cylindrical optics, this requires a specially designed refractive transmission cylinder or computer generated hologram (CGH) that resides in the optical cavity [19–21]. Both types of null correctors can add errors. Errors introduced by refractive null optics include errors in alignment, index of refraction, and surface figure of the lens elements [22]. For CGH nulls, these errors include transmitted wavefront error of the CGH substrate and CGH pattern errors [20]. The performance of null correctors can be estimated based on a bottom-up analysis, but a self-referencing calibration technique is lacking. ASM, implemented here with a CGH null corrector, can be applied to extract the OPD from both the reference surface and null optics, thereby calibrating the system.

2. AXIAL SHIFT MAPPING THEORY

A. Lateral Shearing

Shearing metrology has its roots in multi-sensor probes [9,10], which are shifted as a group. To our knowledge, the first interferometric lateral shearing technique for measuring optical flats

was introduced by Bloemhof [5], which involves taking three measurements, one at a nominal position and then two measurements shifted by one pixel in orthogonal lateral directions. The technique was expanded upon to show that the system could be shifted by more than a single pixel [6]. Unlike the method presented by Bloemhof, ASM for cylindrical surfaces only requires a shift along the axial direction of the mirror. The full surface of the cylinder will be extracted, but radial traces may include influence due to the reference surface and no radial shift.

A Fizeau measurement of a cylindrical surface can be written as

$$M_0(\phi, y) = T(\phi, y) - R(\phi, y), \qquad (1)$$

where T is the surface height map of the SUT, and R is the height produced by the reference surface at the cylindrical coordinates (ϕ, y), with the origin at the center of curvature of the mirror. When null optics are placed in the cavity of the interferometer, their surface height contributions are encompassed by the R term because the optics do not move during a shift. When the SUT is shifted by a distance of Δy, Eq. (1) becomes

$$M_1(\phi, y) = T(\phi, y + \Delta y) - R(\phi, y), \qquad (2)$$

where Δy is along the axial direction of the mirror, and the subscript 1 indicates that it has shifted $1 \times \Delta y$ from the nominal position (Fig. 3). In the shifted measurements, contributions in the interferogram due to the SUT shift, while contributions due to the reference surface are static.

The difference between the shifted map and the nominal map is

(a) Measurement 0: No shift
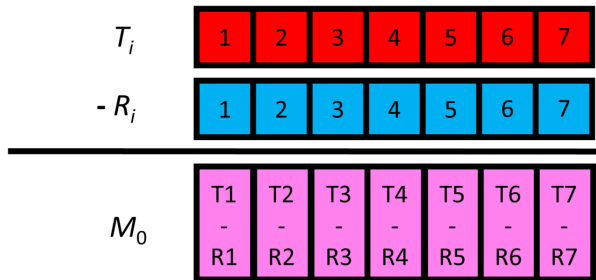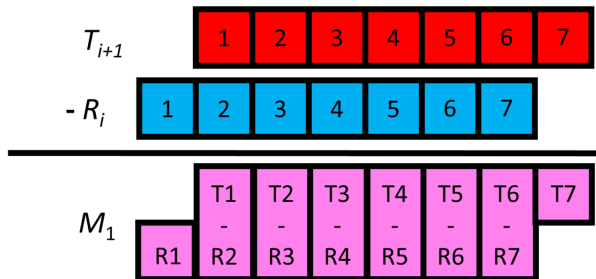

(b) Measurement 1: Δy shift

Fig. 3. Rubric explaining the shifting process. Measurement 0 is taken at the nominal position. The SUT is then shifted along the desired direction by Δy giving measurement 1. The difference between these measurements gives the slope space information of the SUT. This information is integrated to return the surface height of the SUT, which is then used to determine the reference surface.

$$M_1(\phi, y) - M_0(\phi, y) = T(\phi, y + \Delta y) - T(\phi, y), \qquad (3)$$

where contributions due to the reference surface have been eliminated. This represents the slope information of the SUT. To obtain the surface height information, the extracted surface slope information is integrated, or equivalently, solved via a matrix equation.

A Moore–Penrose pseudo inverse matrix [23] is used by setting up the matrix system

$$\mathbf{K}\vec{z} = \vec{m}, \qquad (4)$$

where $\vec{z}$ is a vector containing the true surface height, $\vec{m}$ is a vector containing measurements, and $\mathbf{K}$ is a matrix that relates them through Eq. (3). To describe a single line along a surface, $\vec{z}$ is constructed as

$$\vec{z} = \begin{bmatrix} R_1 & \dots & R_I & T_1 & \dots & T_I \end{bmatrix}^{\mathbf{T}}, \qquad (5)$$

where R_i and T_i are the actual values of the reference surface and SUT, respectively, at pixel i, up to the max number of pixels I. As this is a least mean squares method, the extraction can be performed with more the nominal and shifted measurement by over constraining the system. If we take J measurements, $\vec{m}$ becomes

$$\vec{m} = \begin{bmatrix} m_{1,0} & \dots & m_{I,0} & m_{1,1} & \dots & m_{I,1} & \dots & m_{I,J} \end{bmatrix}^{\mathbf{T}}, \qquad (6)$$

where the first subscript indicates pixel location and the second indicates shift number. Each measurement is concatenated to the end of the previous measurement. The $\mathbf{K}$ matrix is built according to Eq. (3). Solving Eq. (4), $\vec{z}$ is obtained:

$$\vec{z} = (\mathbf{K}^{\mathbf{T}}\mathbf{K})^{-1}\mathbf{K}^{\mathbf{T}}\vec{m}, \qquad (7)$$

which contains the estimated values of the reference surface and the SUT. Since the pseudo-inverse is a least mean squares method, the more the SUT is shifted, the more information is used to extract the surfaces. The number of measurements taken must balance the benefit of more information being used to inform the final surfaces, with physical effects, such as data loss at the edges due to shifting, and changing environmental conditions that cause deformation and measurement drift.

This formulation is for extracting a single line of data. For a surface composed of singular lines of data, the measured and extracted lines are horizontally concatenated in $\vec{m}$ and $\vec{z}$, respectively. The same $\mathbf{K}$ matrix is used for every column, so only one pseudo-inverse matrix must be calculated.

B. Quadratic Ambiguity

During the axial shift, rigid body errors will be introduced. When taking the difference as described by Eq. (3), a rigid body error of a pitch (rotation about x in Fig. 2) of the SUT will create a linearly varying slope measurement. When this linear term is integrated, it presents itself as a quadratic term in the height information. This can mask a true quadratic term in the surface or reference [9]. This section mathematically describes how this quadratic ambiguity, as named by Huang [24], arises and how it is broken with a known artifact mirror (KAM) in the field of view of the interferometer.

1. Origin of the Quadratic Ambiguity

The quadratic ambiguity arises from an inadvertent rotation of the SUT (T) between shifts, the effect of which is indistinguishable from quadratic errors in either the SUT or reference (R). This is illustrated with a simple example of a SUT and reference surface, each represented as purely quadratic surfaces:

$$T_0 = \kappa_T y^2,$$

$$R_0 = \kappa_R y^2, \qquad \text{(8)}$$

where κ is the curvature of the surface. The subscript zero indicates that this is the measurement at the nominal location.

When the test surface shifts laterally by a value of Δy, the surface becomes

$$T_1 = \kappa_T (y + \Delta y)^2 + \theta y, \qquad \text{(9)}$$

where θ is the unknown tilt due to rigid body errors of the stage motion. The measurements are the addition of the reference surface with the test surface:

$$M_0 = \kappa_R y^2 + \kappa_T y^2, \qquad \text{(10)}$$

and

$$M_1 = \kappa_R y^2 + \kappa_T (y + \Delta y)^2 + \theta y. \qquad \text{(11)}$$

The difference between these two measurements, divided by the shifted distance gives

$$\frac{\Delta M}{\Delta y} = \frac{\kappa_R y^2 + \kappa_T (y + \Delta y)^2 + \theta y - (\kappa_R y^2 + \kappa_T y^2)}{\Delta y}, \qquad \text{(12)}$$

which leads to a cancellation of all terms with x^2. This simplifies to

$$\frac{\Delta M}{\Delta y} = \left(2\kappa_T + \frac{\theta}{\Delta y} \right) y + \kappa_T \Delta y. \qquad \text{(13)}$$

The extracted test surface is the integration of this surface:

$$T = \int_0^y \frac{\Delta M}{\Delta y} \mathrm{d}y = \left(\kappa_T + \frac{\theta}{2\Delta y} \right) y^2 + \kappa_T \Delta y y, \qquad \text{(14)}$$

where T is an extracted value. In addition to the $\kappa_T \Delta y$ term (rigid body tilt), an error in the curvature of $\theta / 2\Delta y$ remains. We must therefore measure this tilt θ to accurately reconstruct the surface. In general, real surfaces contain terms of higher order than quadratic, which can also contribute to the quadratic ambiguity.

2. Using the Known Reference to Break the Ambiguity

The tilt introduced during a shift can be measured using a KAM, which is a flat mirror in the field of view of the interferometer. This is an illustrative example of how a KAM is used to break the quadratic ambiguity using a simplified model where the KAM only contains a quadratic term. Before beginning ASM measurements, the KAM is characterized using a three flat test [3]. The KAM is illustrated as a quadratic surface:

$$K_0 = \kappa_K y^2, \qquad \text{(15)}$$

where higher-order terms are ignored. Unlike the two κ terms in Eq. (8), κ_K is known from our three flat test characterization. This KAM is mounted rigidly to the SUT so that any tilts during shifting that affect the SUT also directly affect the KAM. The KAM and SUT are co-aligned to produce fringes in the interferogram at the same time. When a shifted measurement is taken, the KAM surface profile can be described as

$$K = \kappa_K (y + \Delta y)^2 + \theta y + \kappa_R(\phi_K) y^2, \qquad \text{(16)}$$

where $\kappa_R(\phi_K)$ is the curvature of the reference at the azimuthal coordinate of the center line of the KAM. Because the KAM is displaced from the SUT, $\kappa_R(\phi_K)$ is distinct from κ_R. While $\kappa_R(\phi_K)$ is unknown, it will drop out. We rearrange K to become

$$K = \kappa_K y^2 + (2\kappa_K \Delta y + \theta) y + \kappa_K \Delta y^2 + \kappa_R(\phi_K) y^2, \qquad \text{(17)}$$

which has θ contained within known terms. If a line is fit to the measurement of the KAM, the slope is

$$m_K = 2\kappa_K \Delta y + \theta, \qquad \text{(18)}$$

which can be solved to find the tilt θ as

$$\theta = m_K - 2\kappa_K \Delta y, \qquad \text{(19)}$$

whose error is dependent on the error of the KAM curvature measurement and the error of the shift distance. Equation (19) is used to remove relative tilts between measurements. This preserves the linear slope term due to a true quadratic surface. The true measured surface in the presence of rigid body errors can be described as

$$T = \left(\kappa_T + \frac{m_K - 2\kappa_K \Delta y}{2\Delta y} \right) y^2 + \kappa_T \Delta y y, \qquad \text{(20)}$$

which is the surface without a quadratic ambiguity.

C. 2D Quadratic Ambiguity

The quadratic ambiguity arising in lateral shear methods is not contained to a single direction. For a cylindrical SUT, multiple rigid body errors can create a quadratic ambiguity. A model described by Robinson and Reardon states that the surface height error due to a rigid body error of a cylindrical surface, δW, can be described by [25]

$$\delta W = \vec{t} \cdot \hat{n} + \vec{\theta} \cdot (\vec{r} \times \hat{n}), \qquad \text{(21)}$$

where $\vec{t}$ is a vector of the translation $\vec{t} = [\, \epsilon_x \; \epsilon_y \; \epsilon_z \,]^T$, θ is a vector containing the rotations $\vec{\theta} = [\, \theta_x \; \theta_y \; \theta_z \,]$, $\vec{r}$ is the position vector from the center of rotation to each surface location i,

$$\vec{r} = \begin{bmatrix} r_{x,1} & r_{x,2} \ldots r_{x,N} \\ r_{y,2} & r_{y,2} \ldots r_{y,N} \\ r_{z,3} & r_{z,2} \ldots r_{z,N} \end{bmatrix}, \qquad \text{(22)}$$

and $\hat{n}$ is the unit normal vector of the surface. This model assumes $\vec{\theta}$ contains small angles. θ_x corresponds to a pitch rotation of the mirror, which will induce a quadratic ambiguity. θ_z represents a roll rotation of the mirror, and according to Eq. (21) will create an astigmatic height error. This is the equivalent of
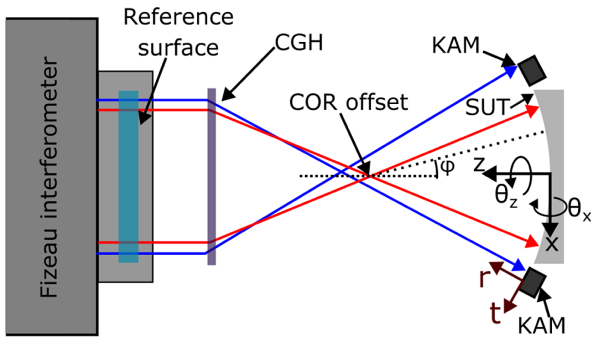
Fig. 4. Diagram of the interferometer and CGH system including the KAMs. The KAMs are tilted at $\pm\phi_K$, and the planar wavefronts for the KAMs come from the opposite side of the cylinder CGH and cross at the cylinder center of curvature. The center of rotation (COR) may be slightly offset due to the choice to offset the KAMs. KAM tilts allow pitch and roll measurements through Eqs. (25) and (26).
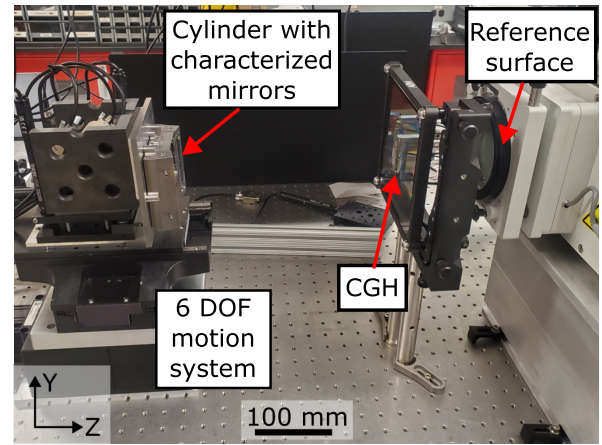

Fig. 5. 2D extraction system including the interferometer with an optical flat as the reference surface, the computer generated hologram (CGH), and the cylinder SUT with the two side mirrors sitting on the 6 deg of freedom (DOF) stage system.

a linearly varying pitch across the surface. For a cylindrical surface, both a pitch and roll will create a quadratic ambiguity in the extracted surface. Therefore, both pitch and roll of the surface during shifting must be measured and subtracted to determine the quadratic term.

To apply ASM to a cylindrical surface, two KAMs are on either side of the SUT, oriented with their normal vectors pointing to the center of curvature of the cylindrical surface, to measure both pitch and roll (Fig. 4). In the global coordinate frame, these KAMs are at azimuthal position $\pm\phi_K$. If a local coordinate frame of (r, s, t) is defined in the center of each KAM with r along the mirror radial direction and t along the azimuthal direction, then every tilt measurement of the KAM will produce a measured rotation about t, θ_t. These rotations directly relate to a pitch, θ_x, and roll, θ_z, of the mirror. If the KAM on the positive x (right) side of the SUT is in the positive ϕ direction, then the measured θ_t of the right and left KAM is, respectively:

$$\theta_{t,R} = \theta_z \sin(\phi_K) + \theta_x \cos(\phi_K), \qquad (23)$$

$$\theta_{t,L} = \theta_z \sin(-\phi_K) + \theta_x \cos(-\phi_K). \qquad (24)$$

The pitch and roll, respectively, are

$$\theta_x = \frac{\theta_{t,R} + \theta_{t,L}}{2\cos\phi_K}, \qquad (25)$$

$$\theta_z = \frac{\theta_{t,R} - \theta_{t,L}}{2\sin\phi_K}. \qquad (26)$$

3. EQUIPMENT AND METHODS

Three separate experiments were performed to test ASM. Each experiment required a slightly altered experimental setup, but all three systems made use of a Fizeau interferometer, an optical flat for a reference surface, a 6 deg of freedom (DOF) motion system for the SUT, and a tip-tilt stage for the CGH. The Fizeau interferometer (Äpre Instruments Inc. S100) has a 2048×2048 pixel detector array. Each pixel is 50.8 μm

square when projected into test space. The interferometer was equipped with a $\lambda/20$ PV transmission flat coated for high fringe visibility with highly reflective surfaces, which served as the reference surface. Each interferometer measurement consisted of 10 phase shifting cycles averaged together. The 6 DOF motion system is composed of multiple independent stages. A separate Z stage (Aerotech AVS100) and XY stage (Aerotech ANT110) handle translational motion. A tip/tilt/rotation stage (Newport 37) with motorized actuators (ThorLabs Z825B) provides rotational motion. All three experiments used Corning ultra-low expansion (ULE) flat mirrors for KAMs (10 mm × 10 mm × 75 mm, coated with a multilayer film for high reflectivity at 633 nm wavelength), but in different orientations. The KAMs were measured using a three flat test, prior to each experiment, after mounting in their respective fixtures. An image of the experimental setup with added components for a 2D extraction can be seen in Fig. 5.

A. 1D Flat Mirror Measurement

Before testing ASM on cylindrical surfaces, we confirmed our ability to extract the surface of a flat mirror, which can easily be compared against a three flat test. This measurement did not use any null corrector, and both the SUT and KAM were nominally flat mirrors of the same dimensions. The SUT and KAM were mounted in the aluminum mount shown in Fig. 6. The KAM was shimmed so that it produced resolvable fringes when the SUT was aligned parallel to the reference surface. Before beginning the measurement, both the SUT and KAM were characterized with a three flat test. This was done after the mirrors were mounted to avoid errors in the characterization due to deformations during mounting.

The SUT and KAM were mounted on the 6 DOF stage system. The stage system was shifted laterally (x) by 100 μm (2 pixels) per shift. Measurements were taken in an alternating scheme, dubbed outside-in. If a measurement at shift location i along a line is described by M_i then the order of measurement would be

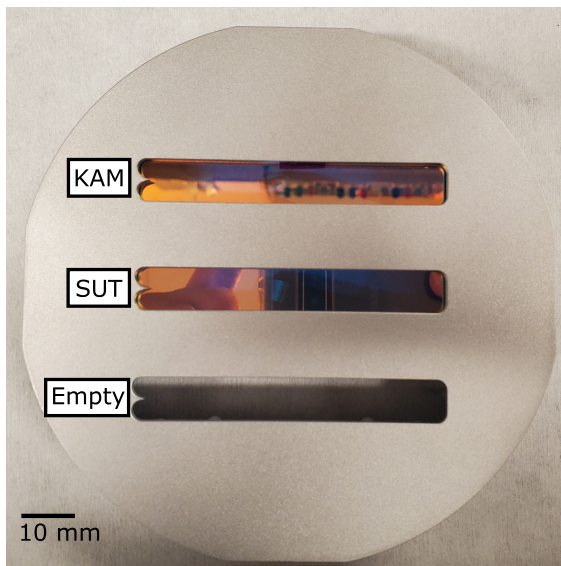$$M_0, M_N, M_1, M_{N-1}, M_2 \dots, \qquad (27)$$

Fig. 6. Mounted ultra-low expansion (ULE) flat SUT and known artifact mirror (KAM) for single line shift mapping extraction. Both the SUT and KAM were characterized using information extracted from a three flat test. A fiducial was added to the mount to ensure the same line was measured during all sets.

which were reordered back to ascending order when analyzing the data. This was done to minimize the effect of any linearly time-varying curvature or relative tilt between the SUT and the KAM, such as temperature.

The full measurement comprised 20 sets of 40 shifts each. The temperature variation during the 20 sets had a peak to valley range of 390 mK. The KAM had a surface figure of 57.3 nm RMS along the center line of the mirror determined from the three flat test. The curvature of the KAM was determined to be $\kappa_K = 1.71 \times 10^{-4}$ m^{-1}.

The relative tilt of each measurement was mathematically removed using the tilt as measured by the KAM, through Eq. (19), where Δy is the distance from the nominal position. The mirrors were not actively aligned during this test. The surfaces were then arranged into the $\vec{m}$ as described by Eq. (6). Because the surface was shifted by two pixels instead of one, the **K** matrix was updated to reflect this change. The pseudo-inverse was taken of this new **K** matrix according to Eq. (7) and multiplied by $\vec{m}$. This produced the decoupled reference surface and SUT.

B. Computer Generated Hologram and Mirror Mounting Geometry

Measuring a cylindrical mirror required a more complex system that generates both a cylindrical wavefront and planar wavefronts for measuring KAM tilts, as well as mounting a cylindrical SUT and two KAMs. A diagram of the setup for cylinder measurements can be seen in Fig. 4. A CGH (produced by Arizona Optical Metrology, LLC) was placed between the reference surface and the SUT, which was designed so the $m = 1$ diffraction order produced the desired wavefronts.

An image of the mirror mount is shown in Fig. 7(a), and a photograph of the CGH can be seen in Fig. 7(b). To mount the
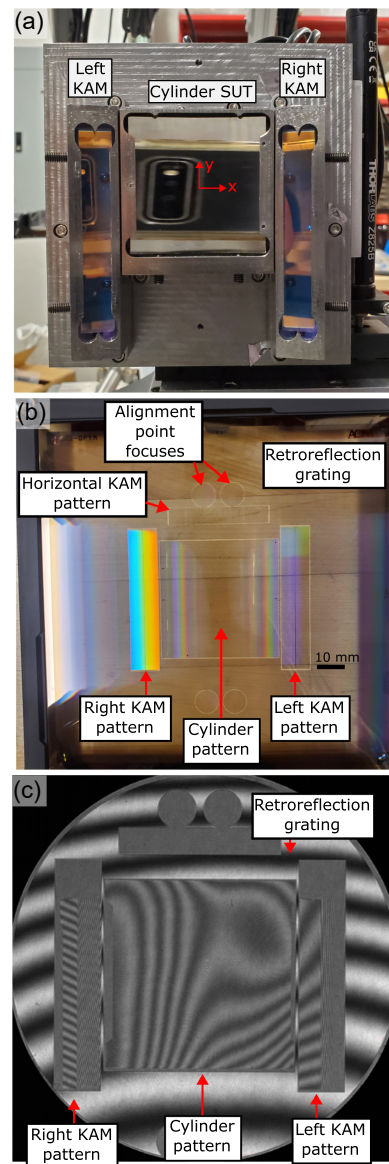

Fig. 7. (a) Photograph of the cylinder mirror with accompanying left and right KAM side mirrors tilted at ±13.9 degrees. Mirrors were mounted in separate capsules to ease alignment. (b) Photograph of the CGH that generates a cylindrical wavefront from the center for the SUT, planar wavefronts for KAMs, and alignment Fresnel zone plates. The KAM patterns are labeled as for their corresponding mirror. The horizontal KAM pattern is not used in this work. (c) Interferogram produced with the CGH and the SUT system. The cylinder was nulled before measurement, but tilt fringes better highlight the CGH regions.

three mirrors, we designed steel capsules that would hold each mirror and mount to a common plate. The cylindrical mirror is mounted in the center, and a KAM is mounted on either side. The two KAMs are angled at $\phi_K = \pm 13.9$ degrees, which allows measurement of the roll. If the KAM was mounted with its optical axis along the interferometer optical axis, the system would measure pitch but be insensitive to roll. The mounting material is steel to balance cost with CTE mismatch between the ULE and mount, compared to aluminium. The SUT is a 50.8 mm by 50.8 mm concave cylindrical mirror with a radius of curvature

of $R = 138$ mm (Newport CSV300), which we coated with 100 nm electron-beam evaporated platinum.

The CGH is a chrome amplitude grating on a fused silica substrate with a <0.1% anti-reflection coating on the back surface. Centered on the CGH is a 50.8 mm by 50.8 mm grating that diffracts light into a cylindrical wavefront that focuses to a line at $f = 138$ mm away and then propagates and matches the $R = 138$ mm of the SUT. On either side of the cylinder pattern is a 60 mm by 5 mm planar wavefront grating that generates a wavefront towards the KAM on the opposite side of the SUT. An interferogram that includes these elements while aligned can be seen in Fig. 7(c). Four alignment Fresnel zone plates produce point foci at the corner of the SUT for rough alignment. In the space between the written gratings is a retroreflection grating that aids in aligning the CGH to the interferometer at the desired angle. There is also a horizontal KAM pattern (along the x direction) that is used for angle measurements in radial extractions, but was not used in the current work.

The planar wavefront holograms for the left and right KAMs have two different patterns. These extra patterns will produce null fringes on the KAMs when the system is shifted around the center of curvature by 0.72 mrad, which is used for radial 2D extraction. The KAMs can be nulled to either the interior or exterior pattern for the corresponding KAM. When an interior pattern is used for one KAM and an exterior pattern is used for the other KAM as seen in the KAM portion of Fig. 7(c), an offset occurs between the measured center of rotation (COR) and axial line focus of the mirror (Fig. 4). Our experimental setup generates a 1.75 mm COR offset when offset patterns are used. This can be compensated for by redefining the normal vectors of the surface in Eq. (21) with this new COR. When both interior and exterior KAM patterns are used, no COR offset occurs.

C. Retrace Error Measurement

We performed a retrace error test to determine the magnitude of the retrace errors due to a misaligned SUT, for both pitch (θ_x) and roll (θ_z). For both tests, a Fizeau measurement was taken at a nominal position, then rotated by 1 µrad around the desired axis using the 6 DOF stage system. The SUT and KAMs were measured again, and 1 µrad steps were repeated for 20 measurements. To evaluate retrace error, the rigid body motions, measured using the KAMs and Eqs. (25) and (26), were removed from all subsequent measurements using Eq. (21), leaving only the retrace error for that angle. With this we could determine if retrace error was a significant error source in the system.

D. 2D Cylindrical Mirror Measurement

After measuring flat mirrors and evaluating the system's retrace error, ASM was applied along the axial direction (y) of a cylindrical surface. This extracted every axial trace of the reference surface and the SUT. As with the 1D surface measurement, the surface shifted in the outside-in sequence as described in Eq. (27). The measurement parameters for the five measurement campaigns of 2D ASM are shown in Table 1.

To mitigate any remaining retrace error and maintain the small angle assumption of Eq. (21), we performed active alignment to mitigate any negative effects due to large tilts during shifting. In the active alignment process, the orientation

Table 1. Measurement Parameters for Separate Campaigns of 2D ASM on a Cylindrical Surface

Campaign	Sets	Measurements Per Set	Pixels Per Shift	Angle Tolerance (µrad)	Offset (mm)
1	10	20	1	1.5	1.75
2	10	20	1	1.5	1.75
3	7	20	1	1	1.75
4	10	20	2	1	1.75
5	10	20	2	1	0

of the SUT is measured using the measured KAM surfaces and Eqs. (25) and (26). Then, the SUT is iteratively rotated about its center using the 6 DOF stage system, until the KAM measurements show that it is within a specified tolerance. The remaining angle is mathematically nulled out though Eq. (21). Due to the active alignment procedure, the total time of measurement is variable with the extra measurements required to align the mirror. For a single set of 20 measurements, a typical measurement time was approximately 20 min.

Both the left and right KAMs were measured after mounting, but prior to performing ASM, using a three flat test. Along the center line, the left KAM had a 259.5 nm RMS surface figure and curvature $\kappa_{K,L} = -8.04 \times 10^{-4}$ m^{-1}, and the right KAM had a 43.9 nm RMS surface figure and curvature $\kappa_{K,R} = -1.34 \times 10^{-4}$ m^{-1}. The measured profiles of the KAMs were used to determine the tilt θ_K, by shifting their profiles by j pixels, subtracting the shifted profiles from the measured profiles at the original position, then calculating the slope. This slope, θ_K, is added to the measured tilt angles $\theta_{t,R}$ and $\theta_{t,L}$ to accurately determine the rigid body tilt of the SUT. During the full set of measurements, the peak to valley temperature variation was 50 mK, so the thermal expansion mismatch between the mirror and its mount has a small effect on the KAM profiles.

The 20 ASM measurements were stacked into one $\vec{m}$ that is L wide by $I \times J$ long, where L is the number of lines on our surface, I is the number of pixels, and J is the number of measurements. A **K** matrix of size ($IJ \times 2I$) was constructed that corresponds to a single- or double-pixel shift for 20 measurements, depending on the measurement campaign. This **K** matrix was inverted using the pseudo-inverse and was multiplied by $\vec{m}$, which calculated our $\vec{z}$. Since this method was only applied along the axial direction, each axial trace is independent, and the mean and best fit line of each trace were removed.

The CGH manufacturer's bottom-up error analysis asserts that transmitted wavefront error (TWE) of the fused silica substrate is the dominant error term of the CGH. To compare ASM against another measurement technique, the TWE of the CGH substrate was measured using spectrally controlled interferometry or SCI (Äpre Instruments SpectrÄ source), which isolates the interference cavity between the two surfaces of the CGH substrate. The optical thickness variation of the substrate is $n(t(x, y) - \bar{t})$ (where $n = 1.457$ is the refractive index of fused silica at $\lambda = 633$ nm, and t is the thickness of the substrate), from which the substrate TWE is $(t(x, y) - \bar{t})(n - 1)/n$ [26]. We compare the SCI-extracted CGH substrate TWE to the ASM measured reference surface to determine the reliability of our method.

The repeatability of ASM was determined through performing multiple ASM shifting procedures on the SUT. Five different measurement campaigns were preformed on the same SUT. The extracted SUT and reference surface of each campaign were then averaged to generate an averaged measured SUT and reference surface. The repeatability is reported as the difference between the five-campaign average and the current campaign.

4. RESULTS AND DISCUSSION

A. 1D Measurement

For the 1D flat mirror measurement, the extracted reference surface line can be seen in Fig. 8, and the extracted SUT line can be seen in Fig. 9. The ASM measurements of the two surface lines were compared against the corresponding three flat test measurement of the same line. The difference at each point was taken, and the standard deviation of the difference surface was calculated. The reference surface as measured by the two techniques has an RMS difference of 2.8 nm RMS, and the SUT has an RMS difference of 3.2 nm RMS. This shows that ASM is
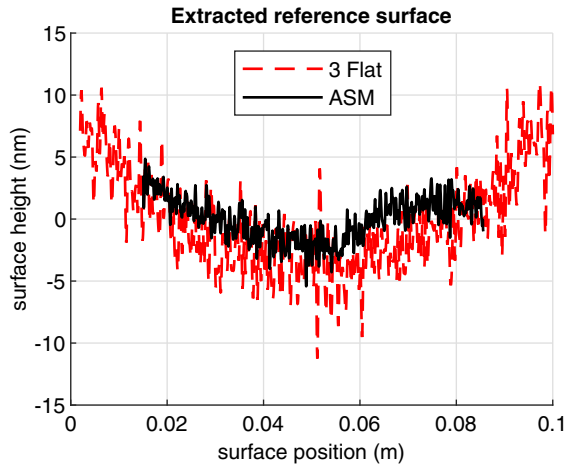

Fig. 8. Reference surface as extracted by axial shift mapping (ASM) and by a three flat test. The RMS difference between the two surfaces is 2.8 nm.
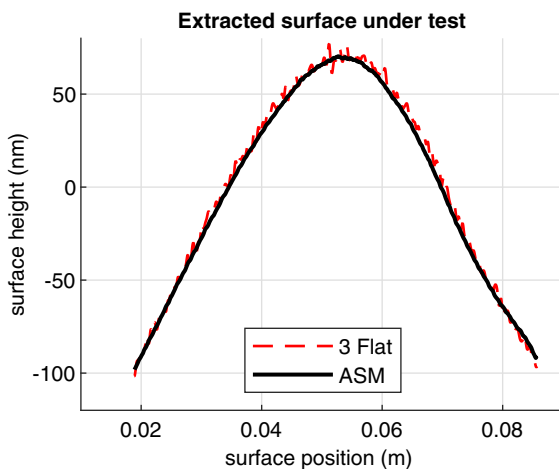

Fig. 9. Test surface as extracted by ASM and by a three flat test. The RMS difference was 3.2 nm.

able to accurately extract both the reference and SUT surfaces as compared to a three flat test for flat surfaces.

B. Retrace Error Measurement

The 20 measurements separated by 1 µrad of angular deviation were performed. Equations (25) and (26) determined the pitch and roll. To determine accuracy, a least-squares model of Eq. (21) was fit to the rotated SUT measurements to independently measure pitch and roll. The measured angles versus the angles determined through fitting for the pitch retrace experiment (Fig. 10) have a difference of 113 nrad RMS. This indicates that KAMs can be used to accurately measure the rigid body errors of the SUT.

The retrace error when rigid body errors are not removed and when they are removed according to the angles as measured by the KAMs was measured. Graphs of both surfaces when rotated by 19 µrad from nominal can be seen in Fig. 11. When rigid body errors are removed, the system has retrace error of 230 nm RMS. When rigid body errors are removed, the system has 6.0 nm RMS of retrace error at 19 µrad of tilt. With the active alignment tolerance set to <1.5 µrad as indicated by Table 1, the retrace error will be even smaller. Therefore, when using KAM based rigid body error removal in conjunction with active alignment, minimal influence due to the retrace error is expected.

C. 2D Cylindrical Mirror Measurement

The five measurement campaigns of the cylindrical surface were carried out according to the parameters as defined in Table 1. The reference surface and SUT were extracted for each campaign through averaging the extracted surface from each set. The extracted reference surface and SUT, as averaged over all five campaigns, are shown in Fig. 12 and Fig. 13, respectively. Comparing the surfaces of each campaign against the five-campaign average, the repeatability for each campaign was calcutated as 4.4 nm RMS for both surfaces (Table 2, columns 1 and 2). The system was less repeatable for a 2 pixel per shift measurement, the cause of which is an avenue for future work.
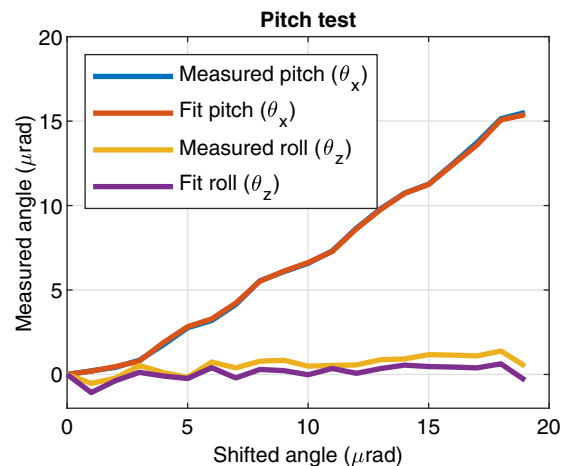

Fig. 10. Pitch and roll, as measured by the KAMs and as measured by fitting Eq. (21) to the surface under test, when varying pitch as described in Section 3.C. The two measurements exhibit 113 nrad RMS difference.
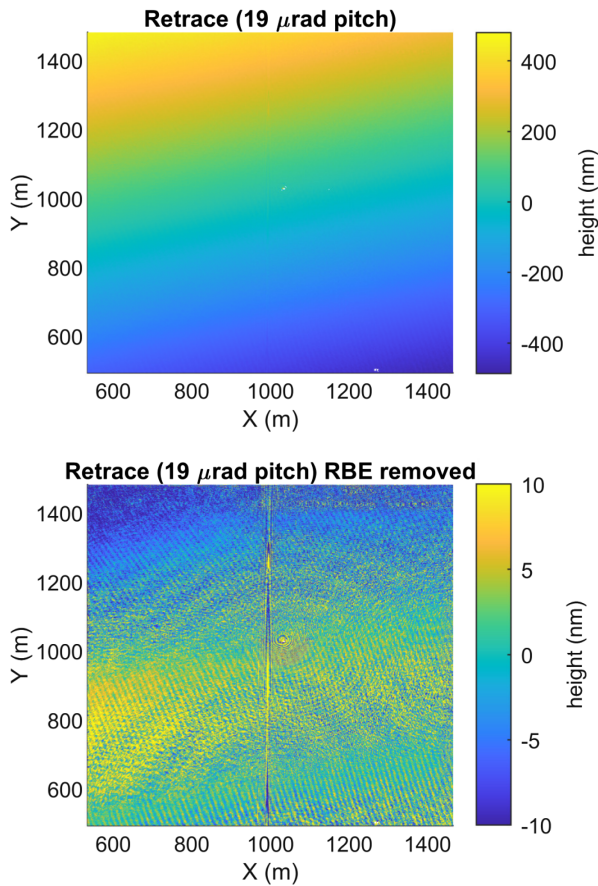
Fig. 11. Retrace error at 19 μrad of pitch (top) without rigid body errors removed and (bottom) with rigid body errors as measured by the KAMs removed. We found that with no rigid body error removal, the surface has retrace error of 230 nm RMS, whereas the removed rigid body error map has 6.0 nm RMS of retrace error.
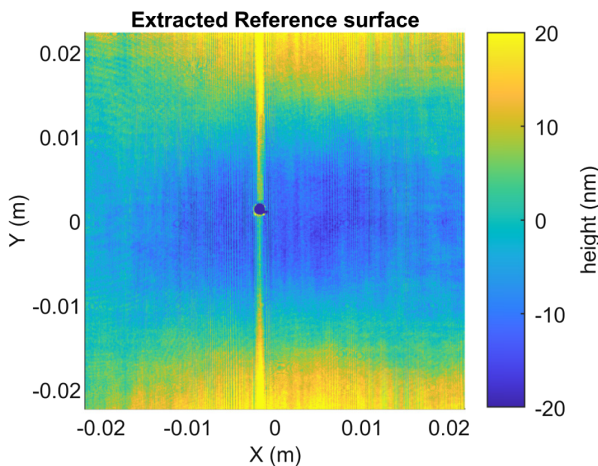

Fig. 12. Reference surface averaged over five measurement campaigns of extraction. The average repeatability of the extracted reference surface is 4.4 nm RMS.

Figure 14 shows the reference surface as extracted through ASM, compared to the CGH substrate TWE as extracted by SCI. There is a column of missing data in the resulting figure, which is due to diffraction effects of the CGH creating unreliable data. The results of these diffraction effects can be
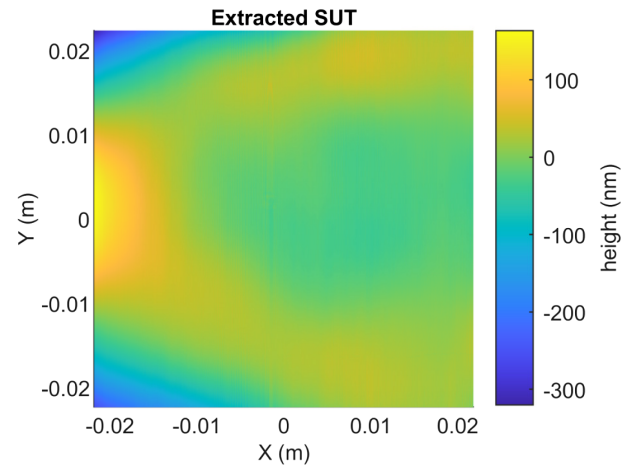

Fig. 13. Test surface averaged over five measurement campaigns of extraction. The average repeatability of the extracted SUT is 4.4 nm RMS.
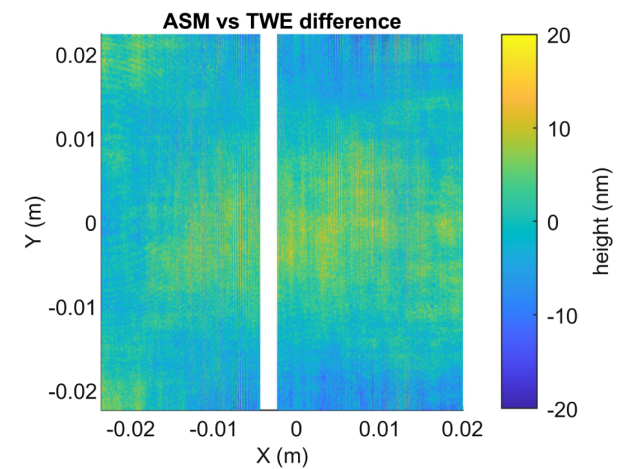

Fig. 14. Difference between the reference surface as extracted through ASM and the CGH substrate transmitted wavefront error as extracted through spectrally controlled interferometry. The average standard deviation of the difference between the two surfaces is 4.5 nm RMS. A vertical line of data is removed due to diffraction effects of the CGH creating unreliable data.

Table 2. Repeatability of the Surface under Test and Reference Surface, and Comparisons between the Reference Surface Using ASM and the Measurement of the CGH Transmitted Wavefront Error

Campaign	SUT Repeatability (nm RMS)	Reference Repeatability (nm RMS)	Comparison (nm RMS)
1	2.7	2.7	4.3
2	1.9	2.7	3.8
3	2.7	2.9	4.5
4	5.2	4.6	5.1
5	9.6	9.2	4.7
Mean	4.4	4.4	4.5

seen in the same column of data in Fig. 12. This surface was generated for all five measurement campaigns, and the standard deviation of this difference can be seen in Table 2 (column 3).

The average standard deviation of the difference between these two surfaces is 4.5 nm RMS. This confirms that the TWE is the dominant factor in the error of the CGH. The remaining error may be due to either ASM or the CGH, from sources such as retrace error, CGH pattern error, reference surface flatness, or inaccuracies introduced from ASM.

5. CONCLUSION

We presented ASM, a self-referencing metrology technique for cylindrical surfaces that can be applied to acylindrical surfaces such as X-ray telescope mirrors. ASM extracts the axial profiles of the SUT and reference surface through shifting the SUT between measurements. This shift induces an inherent quadratic ambiguity due to rigid body errors, and KAMs residing in the field of view of the interferometer were demonstrated to effectively break this quadratic ambiguity. ASM also serves as an end-to-end test of CGH accuracy.

ASM was used to measure one line of a flat mirror, showing 2.8 nm RMS difference compared to a three flat test. The system was extended to measure cylindrical surfaces and measured retrace errors that occur using our KAM based tilt measurement and a CGH, showing 6 nm RMS error at 19 µrad tilt. This confirms that mechanically and mathematically nulling the surface minimizes the effect of retrace errors on the extracted SUT and reference surfaces.

Finally, ASM was applied to cylindrical mirrors. Measuring cylindrical mirrors over five measurement campaigns with varying parameters, surfaces were extracted with a 4.4 nm RMS repeatability. When comparing the extracted reference surface with the independently measured TWE of the CGH substrate, which we expect to be the largest (but not only) error source of the CGH, an average difference of 4.5 nm RMS was found over the five campaigns. The surface extraction of the reference surface confirmed that the transmitted wavefront error is the dominant source. Disagreement between the two surfaces may stem from other smaller error sources such as patterning error or reference surface flatness. Avenues of future work include: investigating error sources that could contribute to the measurement error, expanding ASM to axial and azimuthal surface profile extraction, and expanding to measure X-ray telescope mirrors. To our knowledge, this ASM is the first 2D self-referencing method to measure cylindrical optics including the quadratic term that is so important for X-ray telescope mirrors.

Disclosures. The authors declare no conflicts of interest.

Data availability. Data underlying the results presented in this paper are not publicly available at this time but may be obtained from the authors upon reasonable request.

REFERENCES

1. E. P. Goodwin, *Field Guide to Interferometric Optical Testing* (SPIE, 2006), Vol. **FG10**.

2. G. Schulz and J. Schwider, "Iv interferometric testing of smooth surfaces," in *Progress in Optics*, E. Wolf, ed. (Elsevier, 1976), Vol. **13**, pp. 93–167.

3. U. Griesmann, "Three-flat test solutions based on simple mirror symmetry," Appl. Opt. **45**, 5856–5865 (2006).

4. B. E. Truax, "Absolute interferometric testing of spherical surfaces," Proc. SPIE **966**, 130–137 (1989).

5. E. E. Bloemhof, "Absolute surface metrology by differencing spatially shifted maps from a phase-shifting interferometer," Opt. Lett. **35**, 2346–2348 (2010).

6. E. E. Bloemhof, "Absolute surface metrology with a phase-shifting interferometer for incommensurate transverse spatial shifts," Appl. Opt. **53**, 792–797 (2014).

7. D. Su, E. Miao, Y. Sui, and H. Yang, "Absolute surface figure testing by shift-rotation method using Zernike polynomials," Opt. Lett. **37**, 3198–3200 (2012).

8. Y. Huang, J. Ma, C. Yuan, C. Pruss, W. Sun, M. Liu, R. Zhu, Z. Gao, and W. Osten, "Absolute test for cylindrical surfaces using the conjugate differential method," Opt. Eng. **55**, 114104 (2016).

9. W. Gao, J. Yokoyama, H. Kojima, and S. Kiyono, "Precision measurement of cylinder straightness using a scanning multi-probe system," Precis. Eng. **26**, 279–288 (2002).

10. C. Elster, I. Weingärtner, and M. Schulz, "Coupled distance sensor systems for high-accuracy topography measurement: accounting for scanning stage and systematic sensor errors," Precis. Eng. **30**, 32–38 (2006).

11. L. P. VanSpeybroeck and R. C. Chase, "Design parameters of paraboloid-hyperboloid telescopes for x-ray astronomy," Appl. Opt. **11**, 440–445 (1972).

12. J. A. Gaskin, D. Swartz, A. A. Vikhlinin, *et al.*, "Lynx X-ray observatory: an overview," J. Astron. Telesc. Instrum. Syst. **5**, 021001 (2019).

13. W. A. Podgorski, J. Bookbinder, D. A. Content, W. N. Davis, M. D. Freeman, J. H. Hair, S. M. Owens, R. Petre, P. Reid, T. T. Saha, J. W. Stewart, and W. W. Zhang, "Constellation-X spectroscopy X-ray telescope optical assembly pathfinder image error budget and performance prediction," Proc. SPIE **5168**, 318–333 (2003).

14. P. Takacs, E. Church, S.-N. Qian, and W. Liu, "Development of metrology instruments for grazing incidence mirrors," ISTI-5288804 (Brookhaven National Laboratory, 1989).

15. L. Huang, T. Wang, J. Nicolas, F. Polack, C. Zuo, K. Nakhoda, and M. Idir, "Multi-pitch self-calibration measurement using a nano-accuracy surface profiler for X-ray mirror metrology," Opt. Express **28**, 23060–23074 (2020).

16. A. F. Shipley, W. C. Cash, K. C. Gendreau, and D. J. Gallagher, "Maxim interferometer tolerances and tradeoffs," Proc. SPIE **4851**, 568–577 (2003).

17. B. D. Chalifoux, R. K. Heilmann, H. L. Marshall, and M. L. Schattenburg, "Optical design of diffraction-limited x-ray telescopes," Appl. Opt. **59**, 4901–4914 (2020).

18. P. Uttley, R. den Hartog, C. Bambi, *et al.*, "The high energy universe at ultra-high resolution: the power and promise of x-ray interferometry," Exp. Astron. **51**, 1081–1107 (2021).

19. L. E. Coyle, "Precision alignment and calibration of optical systems using computer generated holograms," Ph.D. thesis (The University of Arizona, 2014).

20. J. H. Burge, "Null test for null correctors: error analysis," Proc. SPIE **1993**, 86–97 (1993).

21. W. W. Zhang, "Manufacture of mirror glass substrates for the NuSTAR mission," Proc. SPIE **7437**, 74370N (2009).

22. J. P. Lehan, T. Hadjimichael, and C. Skocik, "Testing of the mirrors for the constellation-X spectroscopy x-ray telescope with a refractive null," Proc. SPIE **6688**, 668819 (2007).

23. R. Penrose, "A generalized inverse for matrices," Math. Proc. Cambridge Philos. Soc. **51**, 406–413 (1955).

24. L. Huang, T. Wang, J. Nicolas, A. Vivo, F. Polack, M. Thomasset, C. Zuo, K. Tayabaly, D. W. Kim, and M. Idir, "Two-dimensional stitching interferometry for self-calibration of high-order additive systematic errors," Opt. Express **27**, 26940–26956 (2019).

25. B. M. Robinson and P. J. Reardon, "First-order perturbations of reflective surfaces and their effects in interferometric testing of mirrors," J. Mod. Opt. **52**, 2625–2636 (2005).

26. C. Salsbury, "Spectrally controlled interferometry: methods and applications," Ph.D. thesis (The University of Arizona, 2018).